Available online at www.sciencedirect.com
SCIENCE DIRECT
Nuclear Instruments and Methods in Physics Research A 560 (2006) 589–597
NUCLEAR INSTRUMENTS & METHODS IN PHYSICS RESEARCH Section A
www.elsevier.com/locate/nima

X-ray imaging with parametric X-rays (PXR) from a lithium fluoride (LiF) crystal

B. Sones, Y. Danon*, R.C. Block

Gaerttner LINAC Laboratory, Mechanical, Aerospace and Nuclear Engineering Department, Rensselaer Polytechnic Institute, Troy, NY 12180-3590, USA

Received 7 December 2005; received in revised form 17 January 2006; accepted 19 January 2006
Available online 13 February 2006

Abstract

X-ray imaging produced by parametric X-rays (PXR) is reported. The PXR are generated using an electron beam with energy of 56 MeV and currents up to 6.4 μA, that interacted with a 1.5-mm thick lithium fluoride (LiF) crystal target in Laue geometry. The LiF (2 2 0) crystallographic plane was used with a Bragg angle (θ_B) near 15° to produce PXR with energy 16.6 keV and FWHM of 3%. This intense, directional, and tunable X-ray source was then used to image a small fish, an integrated circuit, and an electrical switch with an intensified CCD camera. The bremsstrahlung from the target crystal is characterized as a source of noise and compared to the PXR.

PACS: 41.60.−m; 87.59.−e; 41.75.Fr

Keywords: Parametric X-rays; PXR; LiF; Graphite; Imaging; LINAC

1. Introduction

Parametric X-rays (PXR) are produced from the interaction of relativistic electrons and the periodic structure found in crystalline materials [1]. The first experimental realization of PXR occurred in 1985 [2]. Since then, there have been numerous studies to characterize PXR from Si as well as other materials such as Ge, graphite, and W [3–5]. From these earlier works, PXR is well known as an intense, tunable, quasi-monochromatic, and polarized X-ray source [6]. For medical imaging applications, the traditional X-ray tube, although ubiquitous in hospitals, produces a polychromatic X-ray spectrum that can deliver high dose and suffer from significant scattering as the X-rays penetrate the tissue [7]. According to Dr. Frank Carroll at Vanderbilt University Medical Center, the development of a compact, intense, tunable, narrow bandwidth X-ray source can "open new doors in diagnostic imaging, therapeutics, and biomedical research" [7]. With medical imaging in mind, Kaplin et al. have generated PXR by recycling the 33 MeV electrons of a betatron through target materials such as Si, graphite, and thin multilayer films of W and B_4C [8]. PXR has particular potential in resolving the problems with high false-negative and high false-positive rates associated with conventional mammography systems. PXR can improve image contrast and reduce dose to the patient because its energy tunability allows delivery of an optimal photon energy for a given breast thickness and composition [9]. However, to date there has been no report of PXR imaging in the literature.

In the work presented here, parametric X-rays were used to produce absorption contrast images. This was a proof of principle experiment. The aim of this paper is to discuss this experiment, to characterize the PXR beam used for

*Corresponding author. Tel.: +518 276 4008; fax: +518 276 4832.
E-mail addresses: bryndol.sones@usma.edu (B. Sones), danony@rpi.edu (Y. Danon).

0168-9002/$ - see front matter © 2006 Elsevier B.V. All rights reserved.
doi:10.1016/j.nima.2006.01.054

imaging, and to quantify the bremsstrahlung noise associated with the PXR target crystals. The PXR photon flux was sufficient for X-ray imaging at electron beam currents of a few μA. This novel, intense, tunable X-ray source is promising for any imaging application that requires quasi-monochromatic X-rays.

2. Theory

Parametric X-rays are a continuously tunable X-ray source generated from the interaction of a relativistic electron and the periodic structure of a crystal. The PXR photon energy is effectively independent of the incident electron energy for even moderate electron energies down to 15 MeV, and the photon energy is determined solely by the spacing between crystal planes and by the experimental geometry. The expression for calculating the PXR energy for a given crystallographic plane with a reciprocal lattice vector $\vec{\tau}$ is shown below in Eq. (1) [10].

$$E_{\mathrm{PXR}} = \hbar\omega_{\mathrm{PXR}} = \hbar c \frac{\tau \sin\phi}{1-\cos\Omega}. \tag{1}$$

The electron incident angle (ϕ) is measured with respect to the crystal planes, and the PXR emission angle (Ω) is measured with respect to the electron velocity. Bragg's Law is satisfied for the condition $\Omega = 2\phi$ around which produces the maximum PXR intensity, see Fig. 1

For a given crystallographic plane, the PXR energy can be tuned by rotating the target crystal or by moving the detector while seeking to preserve the Bragg condition for the greatest PXR intensity. The PXR energy linewidth is inherently narrow, limited only by the effective photon lifetime, ~tens of μeV [11]. Energy broadening occurs from parameters of the experiment such as collimator dimensions, crystal thickness, and electron spot size; however, PXR FWHM has been measured as low as 1.2 eV for 4966 eV X-rays (0.024%) [11].

The photon distribution of PXR at positions near the Bragg condition is typically expressed in the solid angle described by angular displacement from the Bragg condition in the diffraction plane (θ_x) and perpendicular to the diffraction plane (θ_y). While it is common to use units convenient for quantum electrodynamics ($h = c = 1$), the MKS expression for the photon distribution of PXR [photons per electron per steradian] is shown in Eq. (2) below [12].

$$\frac{\mathrm{d}^2N}{\mathrm{d}\theta_x\,\mathrm{d}\theta_y} = \frac{\alpha}{4\pi}\frac{\omega}{c}\left[L_{\mathrm{a}}\left|\frac{\hat{n}\cdot\hat{\Omega}}{\hat{n}\cdot\hat{V}}\right|\left(1-\mathrm{e}^{-t/(L_{\mathrm{a}}|\hat{n}\cdot\hat{\Omega}|)}\right)\right] \times \chi^2\mathrm{e}^{-2W}\frac{\theta_x^2\cos^2 2\theta_{\mathrm{B}}+\theta_y^2}{\sin^2\theta_{\mathrm{B}}\left(\theta_x^2+\theta_y^2+\theta_{\mathrm{ph}}^2\right)^2} \tag{2}$$

α is the fine structure constant, ω is the PXR angular frequency, θ_{B} the Bragg angle, and e^{-2W} is the Debye–Waller term which relates to the mean lattice vibration ($\mathrm{e}^{-2W}\sim 1$ at room temperature). The only term related to the electron energy is θ_{ph}, the characteristic angle, which defines the spread of the cone of PXR photons radiated from the crystal. θ_{ph} is approximately $1/\gamma$ (γ is the Lorentz factor) for electron energies less than 100 MeV. χ is the Fourier expansion of the electric susceptibility, which can be viewed as the crystal's diffraction efficiency. The terms in brackets are sometimes referred as the "geometric factor" (f_{geo}), and they relate to the photon absorption along the escape path out of the crystal. $\hat{n}$ is the unit normal to the crystal surface, L_{a} is the absorption length of the PXR in the crystal, and t is the crystal thickness. Both L_{a} and χ depend on the PXR photon energy but in opposing ways; L_{a} increases with photon energy and χ decreases with photon energy.

These competing factors are easily observed when examining theoretical PXR yields for a given crystal thickness while varying the experimental geometry and hence the PXR energy. Fig. 2 shows the calculated lithium fluoride (LiF) (2 2 0) PXR photon yield [photons/e/9 mm^2] in a Laue geometry calculated by integrating Eq. (2) about a 9 mm^2 detector face situated in the diffraction plane, at the characteristic angle, and located 3 m away from the crystal at various Bragg angles. For this calculation, the crystal is rotated while the detector location is moved so that the Bragg condition ($\Omega = 2\phi$) is preserved, and the diffraction plane is perpendicular to the crystal surface $\langle 1\,0\,0\rangle$.

Low Z PXR targets are nicely suited for production of PXR photon energies less than 40 keV because their large

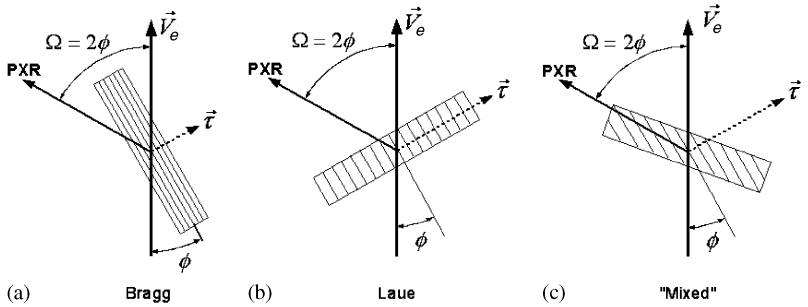

Fig. 1. Different possible PXR emission geometries. The angle between the electron beam velocity vector $\vec{V}_{\mathrm{e}}$ and crystal planes is marked ϕ, $\vec{\tau}$ is the reciprocal lattice vector and the PXR is emitted at an angle $\Omega = 2\phi$ with respect to the electron beam velocity vector.

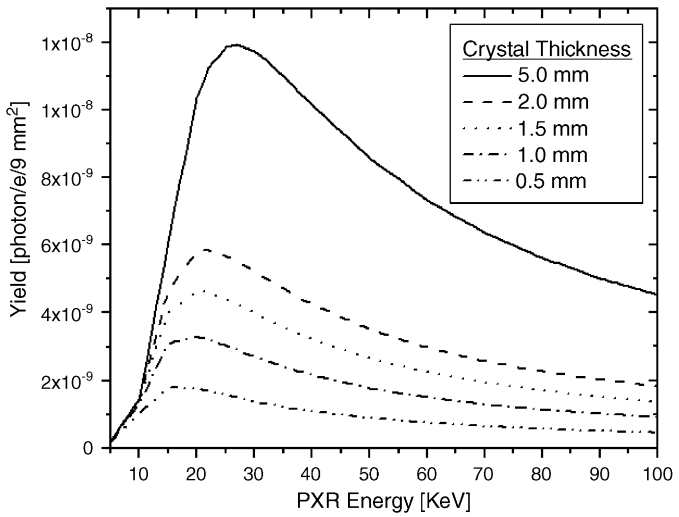

Fig. 2. Calculated LiF (220) PXR yield subtending a 10^{-6} steradian solid angle for various crystals thickness: 0.5, 1, 1.5, 2, and 5 mm. Electron energy is 56 MeV.

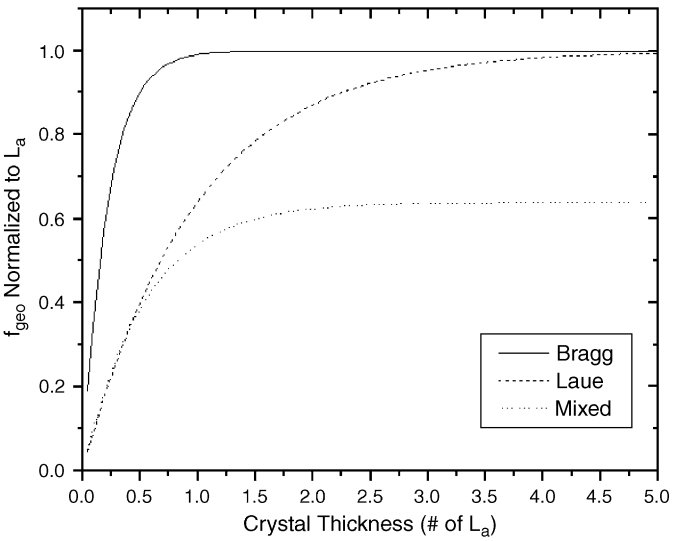

Fig. 3. Calculated geometric factor (f_{geo}) normalized to crystal thickness in units of absorption lengths (L_a) for the Bragg, Laue, and "mixed" crystal geometry, where the mixed geometry has planes at 45° to the crystal surface.

absorption lengths (L_a) allow these photons to escape the target crystal and because the lower Z targets produce less unwanted Bremsstrahlung background. Additionally, LiF has its advantages over other low Z targets such as graphite because graphite's larger mosaic spread and d-spacing. Mosaic spread broadens the PXR energy linewidth and larger d-spacing restricts PXR detection positions closer to the electron beam path for comparable photon energies [13].

In general, the PXR yield increases with crystal thickness up to a point where f_{geo} saturates (neglecting any electron multiple scattering considerations). Any crystal thickness beyond this saturation point only serves to degrade the experiment by increasing the Bremsstrahlung, electron beam divergence, and crystal heating. For different geometries, this saturation occurs at different crystal thicknesses. Fig. 3 shows the normalized f_{geo} calculate for the Bragg, Laue, and a "mixed" geometry for hypothetical crystal planes that are 45° to the crystal surface. The crystal thickness is normalized to numbers of absorption lengths, L_a. The "mixed" geometry [14] is inferior since f_{geo} under this geometry never achieves the maximum level for pure Bragg or pure Laue geometries. The Bragg geometry saturates near a crystal thickness of one L_a, and the Laue geometry saturates near a crystal thickness of four L_a.

The Bragg geometry is most efficient in producing the highest PXR yield. However, with the LiF target crystal used in this experiment, a Laue geometry is preferable to a Bragg geometry because the Laue offers a reduced electron path length in the crystal which results in less Bremsstrahlung production [15]. The electron path length is associated with the crystal thickness and the orientation of the crystal surface to the incident electron beam.

The gains in PXR production from an increase in crystal thickness also increases the crystal's production of Bremsstrahlung, which is viewed as noise for PXR imaging

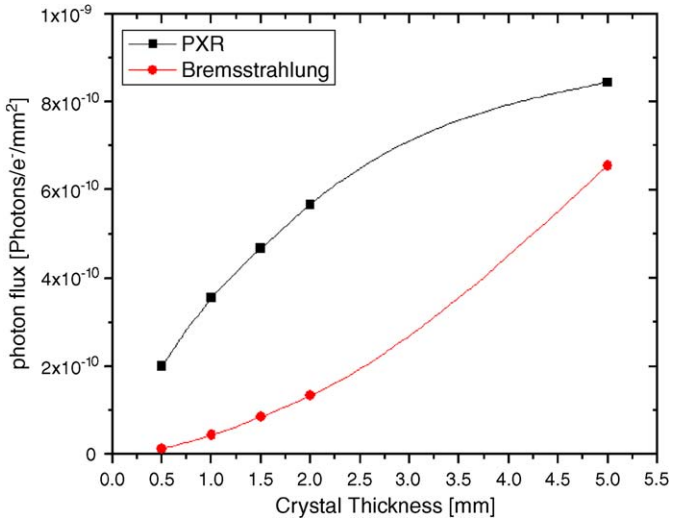

Fig. 4. Comparison of LiF (220) 16.8 keV PXR at a 15° Bragg angle and LiF crystal Bremsstrahlung from 56 MeV electrons.

purposes. Within the narrow energy bandwidth of PXR, this noise is small, but the entire spectrum of Bremsstrahlung energies contributes to the X-ray detector response and degrades the image contrast. Fig. 4 shows a calculation of the PXR and total Bremsstrahlung production for similar experimental conditions. In our experiments, the Bragg angle was 15° resulting in a calculated PXR energy of 16.8 keV at the Bragg condition. This PXR energy is suitable for mammography imaging [16]. Monte-Carlo simulations are performed for a pencil beam of 56 MeV electrons striking the LiF crystal face rotated 15° from the electron direction. Calculated is the total LiF Bremsstrahlung photon flux transmitted through a 3-m air path away to the PXR detector location, 30° off of the electron

Table 1
Collision energy deposition from 60 MeV electrons [17]

Crystal	Collision energy deposition (MeV × cm^2/g)	Density (g/cm^3)	Power deposition (W/μA/cm)
Graphite	1.91	1.70	3.2
LiF	1.74	2.64	4.6
Si	1.87	2.33	4.4

direction. The simulation is limited to photon energies >1 keV, and the total LiF Bremsstrahlung include the energies from 1 keV to 56 MeV. The results of the calculations indicate that as the crystal thickness increases the PXR production increases and reaches a saturation level while the bremsstrahlung production keeps increasing rapidly with the thickness.

The other implication with thicker crystals is in heat deposition. To assess the heating, one can consider the electron energy deposition in the target crystal. Table 1 summarizes 60 MeV electron energy deposition in graphite, LiF, and Si. The selected 1.5 mm LiF crystal heating would be about 0.7 W per μA electron beam current. Thermal lattice vibrations reduce the PXR intensity by the factor e^{-2W} in Eq. (2), this is a relatively small effect (~20% per 500 °K in LiF) [14]. More importantly thermal heating will eventually damage the crystal by cracking or melting it though appropriate cooling can help reduce this effect. In other PXR experiments in the literature, the electron beam currents are typically kept to nA-levels. For this imaging experiment, the current was raised up to 6.4 μA for a short period of time and no crystal cooling was used.

3. Experimental setup

Two detectors are used sequentially in these PXR imaging experiments. The first is an X-ray detector used to optimize the experimental set-up and to gather spectroscopic information about the photons that will be used for imaging. The second detector is a CCD camera that provides spatial information to collect the object image. The RPI PXR experiments begin by passing electrons from the LINAC through a 50 mm diameter by 1.5 mm thick LiF crystal rotated in a 3-axis goniometer to produce PXR directed at a well-collimated, fixed detector location. The X-ray detector is a 500 μm thick Si Amptek XR-100CR detector with 25 mm^2 area and resolution of 350 eV at 17 keV. The detector position is based on the determined Ω (see Eq. (1)) for the required PXR energy. Laser alignment is used to position the detector, crystal, and detector collimation with respect to the LINAC electron beam direction. The LINAC electron beam current is determined from the LINAC pulse rate (typically 400 pulses/s) and the electric charge per pulse measured by a Bergoz Beam Charge Monitor (BCM) concentrically mounted on the electron drift tube. The electron position and spot size/shape are monitored directly on the PXR target crystal

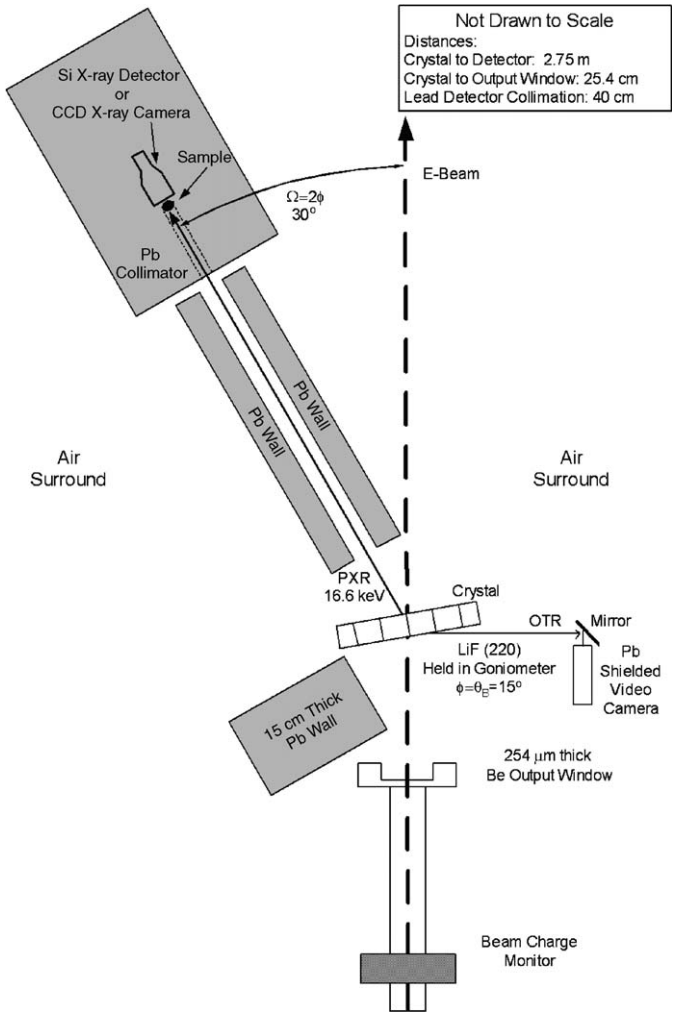

Fig. 5. Experimental set-up for RPI PXR imaging using LiF (2 2 0) in a Laue geometry with Bragg angle of 15°. X-ray detector shown in place for alignment and spectroscopy prior to imaging.

using backward optical transition radiation (OTR) viewed by a distant lead-shielded video camera. Well before the PXR crystal, the electron energy is periodically measured by magnetically bending the electron beam to a Faraday cup. For data shown here, the electron energy is typically 56–60 MeV. Fig. 5 shows the experimental set-up for tuning the PXR production and for measuring the PXR spectrum. The detector is shielded behind a wall of lead with a 40-cm length collimator with area 3 mm × 3 mm. Further lead shielding with 5 cm thickness is placed on either side of the PXR beam path forming a 2.5-cm wide opening extending from the detector collimator entrance back to within about 5 cm from the LiF crystal. An additional 15-cm lead wall is built to shield from bremsstrahlung produced at the output window. Special care is taken to avoid placing the lead in the electron beam. The electron beam spot is focused and positioned appropriately while visually monitoring the OTR from the target crystal. The crystal is then rotated with the goniometer to produce the desired PXR energy with maximum intensity.

For imaging experiments, the PXR is first tuned with the Amptek X-ray detector in place. To image an object, the X-ray detector is then replaced with a 50 mm-diagonal Gemstar intensified gadolinium oxysulfide (15 mg/cm^2) CCD camera with 1392 × 1040 pixel resolution. The small 3 mm × 3 mm lead collimator is replaced with a lead collimator with area 1.6 cm × 1.6 cm such that the center of the CCD camera is placed where the X-ray detector was positioned. Electron currents were in the range from 21 nA for tuning and up to 6.4 μA for imaging, and the electron spot size viewed at the target crystal is approximately 1 cm radius.

4. Results

After PXR tuning, the spectrum was saved to determine the energy and to approximate the intensity of the PXR used for imaging. Fig. 6 shows the PXR spectrum collected with the small 3-mm collimator and with the electron beam current at 21 nA.

There are three discernable peaks in the spectrum. The first (16.63 keV) corresponds to the first order, LiF (2 2 0), PXR peak; the second (33.25 keV) corresponds to the second order, LiF (4 4 0), PXR peak; and the third (39 keV) referred as the ''saturation peak'' corresponds to the binning of all counted photons with energy greater than 39 keV placed in the last channel of the multi-channel analyzer. The spectrum was collected with electron beam current of 21 nA on the crystal for 120 s. Raw data are presented in Table 2.

Some comments about Table 2 are necessary. First, the measured energies of the first- and second-order PXR peaks are multiples of each other as expected. Second, while the experimental set-up was laser aligned for a 15° Bragg angle, the corresponding angles for the measured energies were consistently 15.17°, indicating that the

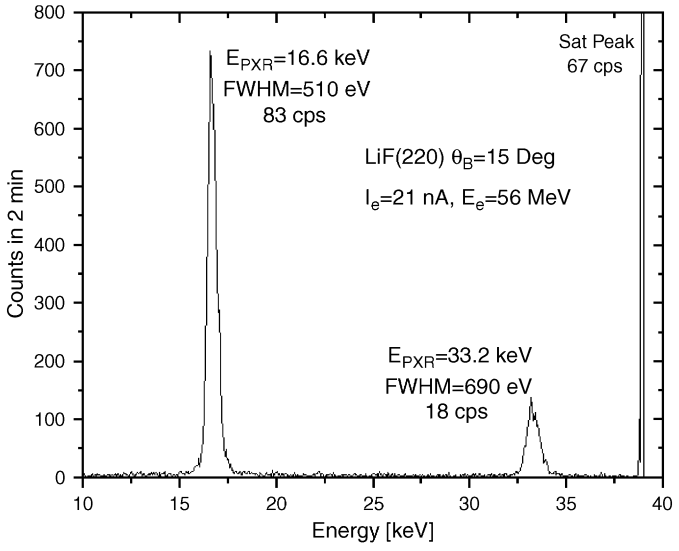

Fig. 6. LiF (220) PXR spectrum measured with 3 × 3 mm^2 collimation and 21 nA electron beam current.

Table 2
Data summary from LiF (2 2 0) spectrum shown in Fig. 6

Peak	Measured energy (keV)	Bragg angle (deg)	Net count rate (cps)	FWHM (eV)	Background (cps)
(2 2 0)	16.63	15.17	82.9	510	3.5
(4 4 0)	33.25	15.17	18.3	690	1.6
Saturation	>39	NA	66.8	NA	NA

precision in laser alignment is to within about 0.2°. Third, the net count rate for the second-order PXR peak was predictably smaller than the first-order PXR peak with an observed ratio of about 1–4, although theoretically calculated values would indicate that the second-order should be closer to two orders of magnitude smaller. In other PXR experiments using near absorption edge transmission experiments [18], we have found that the counts measured in the second-order peak are first-order pile-up events. Finally, the background under the first-order peak is only 5%. As seen in the PXR spectrum in Fig. 6, the total count rate in this spectrum was 197 cps with 101 cps in the two PXR peaks and 96 cps remaining as background photons count rate. The measured ratio of LiF (2 2 0) PXR photons to LiF Bremsstrahlung background photons is then about 1 while the calculation results shown in Fig. 4 would suggest a ratio of about 5. This situation might indicate that some of the saturation counts are due to high-energy photons produced in the electron beam path of the accelerator and reach the detector by penetrating the lead shield. These last two issues regarding the relative yields and the high-energy Bremsstrahlung need further investigation.

Now consider the impact of the changes made to produce the PXR images. For the imaging part of this experiment, the X-ray detector is replaced with a CCD camera; the electron beam current is increased; and the detector collimator opening is increased to 1.6 cm × 1.6 cm. At higher electron beam currents, the mean PXR energy is assumed to remain the same since there are no changes to the experimental alignment, but one can expect a larger energy distribution (FWHM) in changing the collimator from a width of 3 mm to 1.6 cm. PXR energy broadening is determined by geometric factors, $\delta\theta_{\mathrm{geo}}$, and the crystal mosaic spread, α, [19] as shown in Eq. (3) in which the geometric factors are dominated by the detection collimation angle.

$$\left.\frac{\delta E_{\mathrm{PXR}}}{E_{\mathrm{PXR}}}\right|_{\mathrm{tot}} = \cot\theta_{\mathrm{B}}\sqrt{\alpha^2+(\delta\theta_{\mathrm{geo}})^2}. \quad (3)$$

The electron beam experiences multiple scattering events that contribute to the uncertainty of the electron incident angle, $\delta\phi$. The Gaussian standard deviation from each scattering material can be analytically calculated [11]. The scattering medium have the following impact: the 254 μm (10 mil) Be output window (~3 mrad), the 25 cm air path to the crystal (~3 mrad), and the 1.5 mm thick target crystal

(~13 mrad) contributing $\delta\phi$~14 mrad when added in quadrature. Propagating the electron incident angle uncertainty in Eq. (1), this electron beam divergence alone would result in energy linewidth broadened to 5%. We have not observed this level of energy broadening with the 1.5 mm thick LiF crystal as shown in Fig. 6. Polyitsyn argued that the collimator dimension and mosaicity dominate the PXR energy broadening while the electron divergence has little impact [19]. Our data supports this conclusion so we are primarily concerned with the collimator effects on energy broadening. The increase in the collimator size increases $\delta\Omega$ from 0.6 to 2.9 mrad in the worst-case scenario of having a point-like electron beam spot. This contributes to a calculated change in energy linewidth from 0.1% to 0.5%. As a side note, the 3% energy linewidth observed in Fig. 6 is primarily attributable to the detector resolution. The Amptek XR-100CR 500 μm Si detector has a resolution of 350 eV at 17.5 keV [20]. The actual PXR energy linewidth in our experiments is much smaller and has been measured as small as ~45 eV at 8.96 keV (0.5%) by scanning Si (4 0 0) PXR about the K-edge of copper and fitting the measured transmission with a calculated transmission broadened with a Gaussian distribution [21].

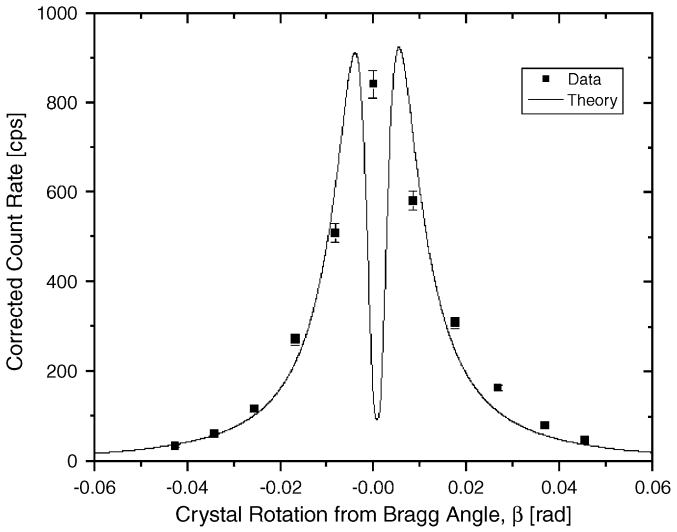

Fig. 7. Absolute LiF (220) PXR count rates measured from a fixed detector angle $\Omega = 30.4^\circ$ while rotating the crystal about the Bragg angle $\phi = 16.2^\circ$. Corrections made for detector deadtime, detector efficiency, and PXR loss in air. Electron current is 1.5×10^{11} e/s.

The next consideration is with the photon intensity used for imaging. First, the data shown in Table 2 must be corrected for detector deadtime. Shown below is a useful model for any pulsed spectroscopy application that can correct for deadtime using three measured quantities: spectrum count rate (PXR_{data}), total count rate ($Total_{data}$), and the frequency of the pulsing (f) [22]

$$PXR_{Corrected} = \frac{PXR_{Data} f}{f - Total_{Data}}. \quad (4)$$

With a LINAC repetition rate of 400 pulses/s, the corrected 16.6 keV count rate at 21 nA is 18.2 photons/s/mm^2. To characterize the PXR photon distribution, the target crystal was rotated an angular displacement of β from the Bragg angle while measuring the PXR count rate at the stationary X-ray detector. The crystal angular displacement of β from the Bragg angle ($\phi = \theta_B + \beta$) changes the detector Bragg condition by 2β ($\Omega = 2\theta_B + 2\beta$) where θ_B is the original Bragg angle. Fig. 7 shows PXR count rate data corrected for detector deadtime, detector efficiency, and photon absorption along the actual 274-cm air pathway to the detector. The solid line in Fig. 7 is calculated without applying any photon distribution broadening. This calculation integrates Eq. (2) about the detector solid angle with an angular shift of 2β in the integration limits of θ_x. All energy-dependent variables in Eq. (2) were appropriately changed to correspond to the new PXR energy. Analogous to a rocking curve, the data agrees nicely with the width of the predicted distribution. In agreement with Potylitsin's theoretical model [19], consideration of the PXR photon distribution broadening effects serves to only fill in the central minima at the Bragg angle while retaining the unbroadened width of the PXR distribution. Potylitsin's theoretical model [19] has also been validated under these experimental conditions to

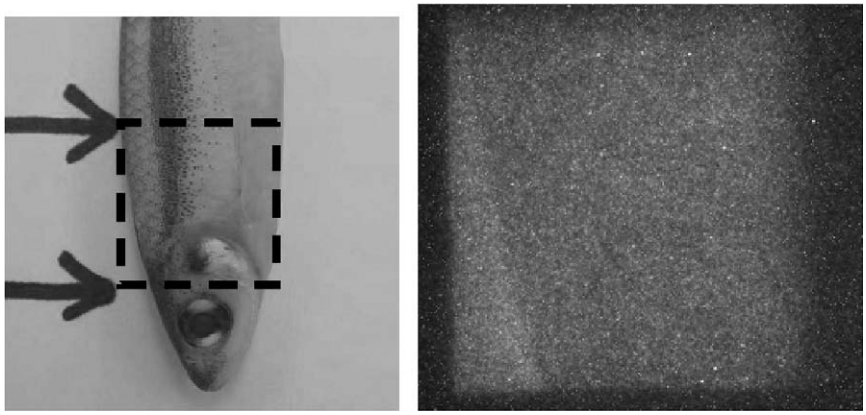

Fig. 8. Photograph and background CCD image of 7.5 cm long fish bait at 2.6 μA electron beam current with 15 s exposure. PXR crystal rotated 5° from Bragg angle for background image.

make absolute PXR photon yields [23]. A simple transformation of the data in Fig. 7 can provide information about the photon distribution at the detector in the diffraction plane under the Bragg condition. We estimate that the FWHM of the PXR beam at the detector location is 12 cm. Then, the intensity variation in the large collimator (1.6 cm × 1.6 cm) is considered uniform with less than 1% variation between the collimator edges in the diffraction plane. The energy variation is 200 eV from edge to edge.

The measurement of PXR with small crystal rotations from the Bragg angle was also used to verify that the measured spectrum is PXR rather than diffraction of Bremsstrahlung incident on the crystal since the two sources have diverging energies as the crystal is rotated farther from the Bragg angle [13,24].

Fig. 9. PXR image of fish bait shown in Fig. 8, 2.6 μA electron beam current with 15 s exposure.

Finally, the increase in beam current would predict a linear increase in photon yield with a small correction for thermal vibration. This effect is the e^{-2W} term in Eq. (2), and the impact can be calculated with the temperature of the crystal and its Debye temperature [25]. For the LiF crystal, the Debye temperature is 730 K and the melting temperature is 1140 K. The crystal temperature was not monitored during this experiment; the LiF crystal did not melt, so as a conservative estimate, we can assume that the crystal temperature remained below 600 K in the few minutes that the current was raised to μA levels. At that temperature, the Debye factor would reduce the photon yield to about 80% of the room temperature value. Then, the photon yield at 6.4 μA would scale to about 4,400 photons/s/mm^2 inside the area of the 1.6 cm x 1.6 cm collimator.

Now with some characterization of the PXR used for imaging, we can discuss the three images presented in this paper. In the Figs. 8, 10 and11, a digital photograph of the imaged object is shown on the left and the X-ray image recorded by the Photonic Science Gemstar CCD camera is shown on the right. A dashed box on the photograph identifies the approximate area of the X-ray image. Exposure times are typically 15–25 s, and the CCD image intensifier gain is generally kept low in order to minimize pixel saturation. As a matter of routine, recorded images are compared to images observed with detuned PXR in order to verify that the recorded image is attributable to the 16.6 keV PXR and not to background X-rays. PXR detuning was accomplished by rotating the crystal 5 degrees from Bragg angle eliminating the PXR produced at the object location. The imaged objects are a small fish

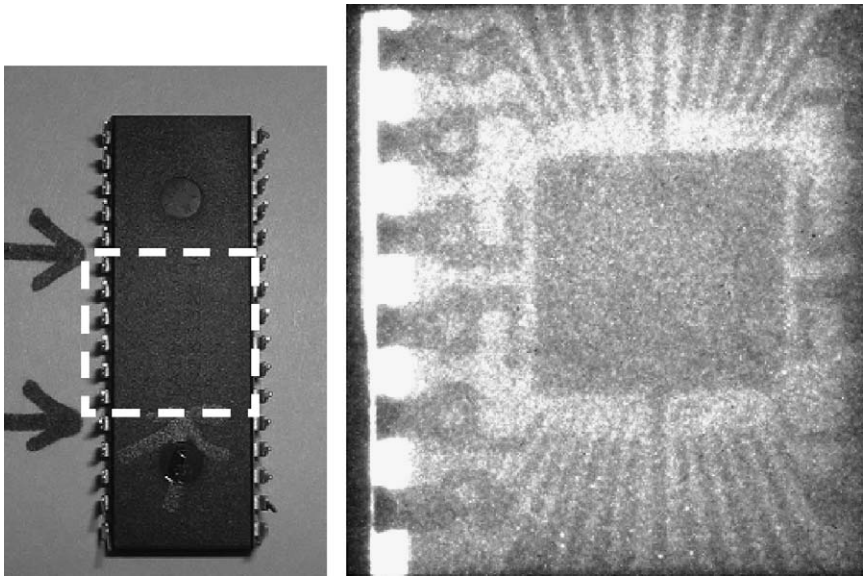

Fig. 10. Photograph and PXR image of cm long computer chip at 3.2 μA electron beam current with 25 s exposure.

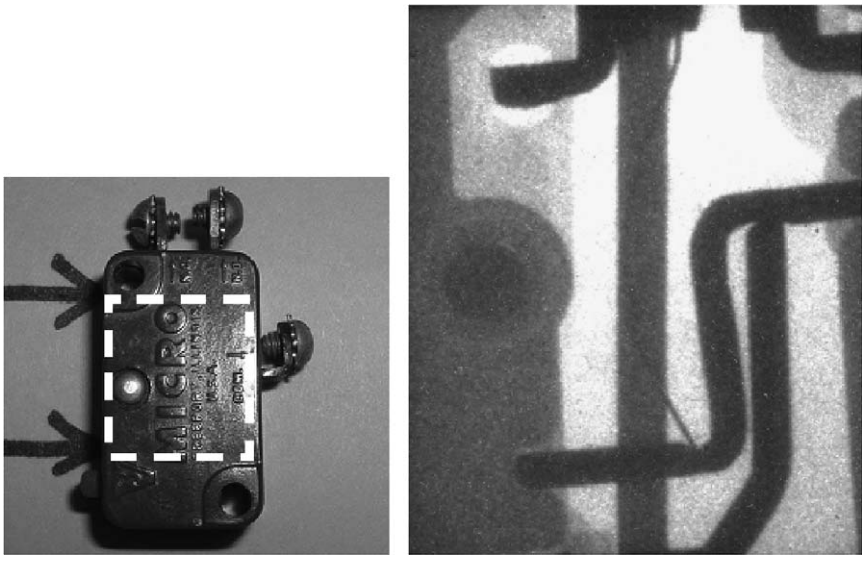

Fig. 11. Photograph and PXR image of 2.5 cm long electrical switch at 6.4 μA electron beam current with 20 s exposure.

purchased as bait from a retailer, PC-BIOS computer chip, and micro switch.

In Fig. 8, the X-ray image (at right) is formed with the PXR detuned by rotating the LiF crystal 5° from the Bragg angle. This background image shows only the outline of the fish body and no internal structure.

Fig. 9 shows the fish image with the LiF crystal at the Bragg angle. In this PXR image, the fish spine is clearly visible with smaller lateral bones extending outward from the spine and with gills surrounding the head area.

Two additional objects were imaged during this first PXR imaging experiment. Figs. 10 and 11 show images of a computer chip and a micro switch, respectively, exposed with PXR from LiF (2 2 0).

5. Conclusions

This work was a proof of principle demonstration that an adequate PXR photon flux can be achieved to produce X-ray images. While PXR has been produced for nearly 20 years, to our knowledge there has been no report of X-ray images generated from PXR. A thick 1.5 mm LiF (2 2 0) in the Laue geometry was the target crystal for 56 MeV electrons from the Rensselaer linear accelerator. Experiments were done in two phases: PXR optimization at a low electron beam current of 21 nA with an X-ray detection system, followed by PXR imaging at high electron beam currents up to 6.4 μA with an intensified CCD X-ray camera. Three objects were imaged: a small fish, a PC-BIOS computer chip, and a micro switch. Presented were techniques for scaling spectroscopic measurements made with a small detector collimator and at low electron beam current to the conditions used for imaging. And a qualitative discussion was provided about the measured PXR photon distribution measured by the CCD camera.

Further work is needed to realize the imaging potential of PXR. This includes resolving the discrepancy between measured and calculated relative yield for LiF (2 2 0) and LiF (4 4 0); improving the characterization of high-energy photons (>39 keV) generated from the crystal; and developing an alternative electron beam current monitor. The CCD camera background must be adequately measured. It is necessary to make CCD measurements of the direct, un-attenuated PXR distribution and the transmission of various known absorbers. Finally, the target crystal must be cooled in order to make full use of the Rensselaer maximum electron beam current of 200 μA.

References

[1] M.L. Ter-Mikaelian, High Energy Electromagnetic Processes in Condensed Media, Wiley-Interscience, New York, 1972.
[2] V.G. Baryshevshy, et al., Angular distribution of parametric X-rays, Phys. Lett. 110A (1985) 447.
[3] A.V. Shchagin, V.I. Pritupa, N.A. Khizhnyak, A fine structure of parametric X-ray radiation from relativistic electrons in a crystal, Phys. Lett. A 148 (1990) 485.
[4] E.A. Bogomazova, B.N. Kalinin, G.A. Naumenko, D.V. Padalko, A.P. Potylitsyn, A.F. Sharafutdinov, I.E. Vnukov, Diffraction of real and virtual photons in a pyrolytic graphite crystal as source of intensive quasimonochromatic X-ray beam, Nucl. Instr. and Meth B 201 (2003) 276.
[5] Y. Adischev, S. Arishev, A. Vnukov, A. Yukolov, A. Polyitsyn, S. Kuznetsov, V. Zabaev, B. Kalinin, V. Kaplin, S. Uglov, A. Kubankin, N. Nasonov, Angular distribution of X-ray radiation by 500 MeV electrons in an tungsten crystal, Nucl. Instr. and Meth B 201 (2003) 114.
[6] P. Rulhusen, X. Artur, P. Dhez, Novel Radiation Sources Using Relativistic Electrons, from Infrared to X-rays, World Scientific Series on Synchrotron Radiation Techniques and Applications, vol. 4, World Scientific, Singapore, 1998.
[7] F. Carroll, Tunable monochromatic X-rays: an enabling technology for molecular/cellular amaging and therapy, J. Cell. Biochem. 90 (2003) 502.

[8] V. Kaplin, S. Uglov, O. Bulaev, V. Goncharov, A. Voronin, M. Piestrup, C. Gary, N. Nasonov, M. Fuller, Tunable, monochromatic X-rays using the internal beam of a betatron, Appl. Phys. Lett. 80 (18) (2002) 3427.
[9] M.A. Piestrup, X. Wu, V.V. Kaplan, S.R. Uglov, J.T. Cremer, D.W. Rule, R.B. Fiorito, A design of mammography units using a quasimonochromatic X-ray source, Rev. Sci. Instrum. 72 (4) (2001) 2159.
[10] T. Akimoto, M. Tamura, J. Ikeda, Y. Aoki, F. Fujita, K. Sato, A. Honma, T. Sawamura, M. Narita, K. Imai, Generation and use of parametric X-rays with an electron linear accelerator, Nucl. Instr. and Meth A 459 (2001) 78.
[11] K.H. Brenzinger, B. Limburg, H. Backe, S. Dambach, S. Euteneuer, F. Hagenbuck, C. Herberg, K.H. Kaiser, O. Kettig, G. Kube, W. Lauth, H. Schope, Th. Walcher, How narrow is the linewidth of parametric X-ray radiation?, Phys. Rev. Lett. 79 (1997) 2462.
[12] J. Freudenberger, H. Genz, V. Morokhovshyi, A. Richter, J. Sellschop, Parametric X-rays observed under Bragg condition boost of intensity by a factor of two, Phys. Rev. Lett. 84 (2) (2000).
[13] B. Sones, Y. Danon, R.C. Block, Lithium fluoride (LiF) crystal for parametric X-ray production, submitted for publication Radiation from Relativistic Electrons in Periodic Structures (RREPS 03) Proceedings, Nucl. Instr. and Meth B 227 (2005) 22.
[14] B. Sones, Production of intense, tunable, quasi-monochromatic X-rays using the RPI linear accelerator, Ph.D. Thesis, Rensselaer Polytechnic Institute, www.osti.gov/servlets/purl/835860-Id25lw/native/ 2004.
[15] B. Sones, Y. Danon, R. Block, Lithium Fluoride crystal advantages in parametric X-ray (PXR) production, in: Proceedings of the ANS Winter Meeting, New Orleans, LA, 2003.
[16] A.B. Wolbarst, Physics of Radiology, Medical Physics Publishing, Madison, WI, 2000.
[17] Estar Web site http://physics.nist.gov/PhysRefData/Star/Text/ESTAR.html
[18] B. Sones, Production of intense, tunable, quasi-monochromatic X-rays using the RPI linear accelerator, Ph.D. Dissertation, Rensselaer Polytechnic Institute, 2005.
[19] A.P. Potylitsin, Influence of beam divergence and crystal mosaic structure upon parametric X-ray radiation characteristics, arXiv: cond-mat/9802279 v1, 26 February 1998.
[20] Amptek, Inc. Operating Manual, XR-100CR, X-ray Detector.
[21] B. Sones, Y. Danon, R. Block, Advances in parametric X-ray production at the RPI linear accelerator, in: Proceedings of the ANS Annual Meeting, San Diego, CA, June 2003.
[22] Y. Danon, B. Sones, R.C. Block, Dead time and pileup in pulsed parametric X-rays spectroscopy, Nucl. Instr. and Meth. A 524 (2004) 287.
[23] B. Sones, Y. Danon, R. Block, The effects of electron scattering on the absolute parametric X-ray (PXR) yield calculations, in: ANS Annual Meeting, San Diego CA, June 2005.
[24] A.V. Shchagin, V. I. Pristupa, N. A. Khizhnyak, Absolute differential yield of parametric X-rays radiation, in: Proceedings of the International Symposium of Radiation from Relativistic Electrons in Periodic Structures, 6–10 September 1993, Tomsk, Russia.
[25] K.Yu. Amosov, B.N. Kalinin, A.P. Potylitsin, V.P. Sarychev, S.R. Uglov, V.A. Verzilov, S.A. Vorobiev, I. Endo, T. Kobayahsi, Influence of temperature on parametric X-ray intensity, Phys. Rev. E 47 (3) (1993).